Chinese Physics Letters

EXPRESS LETTER

$Cs_3V_9Te_{13}$: A New Vanadium-Based Material with a Reuleaux-Triangle-Like Lattice and a Possible Phase Transition near 48 K

Cite as: Zhen Zhao *et al*. 2026 *Chin. Phys. Lett.* **43** 060703

DOI CSTR

Recommended Articles

Emergent Fermi-Liquid-Like Phase by Melting a Holon Wigner Crystal in a Doped Mott Insulator on the Kagome Lattice
Xu-Yan Jia, Wen Huang, D. N. Sheng, and Shou-Shu Gong
Chin. Phys. Lett. **43**, 030706 (2026)

Emergence of Superconductivity on the Border of Antiferromagnetic Order in RbMn$_{6}$Bi$_{5}$ under High Pressure: A New Family of Mn-Based Superconductors
Peng-Tao Yang, Qing-Xin Dong, Peng-Fei Shan, Zi-Yi Liu, Jian-Ping Sun, Zhi-Ling Dun, Yoshiya Uwatoko, Gen-Fu Chen, Bo-Sen Wang, and Jin-Guang Cheng
Chin. Phys. Lett. **39**, 067401 (2022)

A Possible Quantum Spin Liquid Phase in the Kitaev–Hubbard Model
Shaojun Dong, Hao Zhang, Chao Wang, Meng Zhang, Yong-Jian Han, and Lixin He
Chin. Phys. Lett. **40**, (2023)

Ultrafast Carrier Dynamics in $Ba_6Cr_2S_{10}$ Modified by Toroidal Magnetic Phase Transition
Litong Jiang *et al*.
Chin. Phys. Lett. **41**, (2024)

A New Superconductor Parent Compound NaMn$_{6}$Bi$_{5}$ with Quasi-One-Dimensional Structure and Lower Antiferromagnetic-Like Transition Temperatures
Ying Zhou, Long Chen, Gang Wang, Yu-Xin Wang, Zhi-Chuan Wang, Cong-Cong Chai, Zhong-Nan Guo, Jiang-Ping Hu, and Xiao-Long Chen
Chin. Phys. Lett. **39**, 047401 (2022)

A series journal of Chinese Physical Society distributed by IOP Publishing

Chinese Physics Letters

Chin. Phys. Lett. **43** 060703 (2026)

EXPRESS LETTER

DOI: 10.1088/0256-307X/43/6/060703
CSTR: 32039.14.0256-307X.43.6.060703

$Cs_3V_9Te_{13}$: A New Vanadium-Based Material with a Reuleaux-Triangle-Like Lattice and a Possible Phase Transition near 48 K

Zhen Zhao(赵振)[1,†], Jianping Sun(孙建平)[1,2,†], Xin-Wei Yi(易鑫伟)[3,†], Tong Liu(刘童)[2,†], Lin Zhu(朱林)[1], Hanming Ma(马翰明)[1,2], Ruwen Wang(王汝文)[1,2], Hua Zhang(张华)[1,2], Yuhang Zhang(张宇航)[1], Haisen Liu(刘海森)[1], Xiaoli Ma(马肖莉)[1,2], Hui Guo(郭辉)[1,2], Xiao Lin(林晓)[2], Lihong Bao(鲍丽宏)[1,2], Xiaohui Yu(于晓辉)[1,2], Wu Zhou(周武)[2], Jinguang Cheng(程金光)[1,2,*], Gang Su(苏刚)[3,*], Haitao Yang(杨海涛)[1,2,*], and Hong-Jun Gao(高鸿钧)[1,2,*]

[1]Beijing National Center for Condensed Matter Physics and Institute of Physics, Chinese Academy of Sciences, Beijing 100190, China
[2]School of Physical Sciences, University of Chinese Academy of Sciences, Beijing 100190, China
[3]Institute of Theoretical Physics, Chinese Academy of Sciences, Beijing 100190, China

[†]These authors contributed equally to this work.
[*]Corresponding authors. Email: jgcheng@iphy.ac.cn; sugang@itp.ac.cn; htyang@iphy.ac.cn; hjgao@iphy.ac.cn

Exploring and synthesizing materials with new crystal structures provides an important route to discovering exotic quantum phenomena. However, materials with unconventional lattice geometries remain largely unexplored. Here, we report the discovery of a new vanadium-based material, $Cs_3V_9Te_{13}$, featuring a Reuleaux-triangle-like lattice composed of interwoven triangular, square, and pentagonal motifs. Electrical transport, Hall, and magnetic measurements consistently reveal an anomaly near 48 K, and this feature shows little sensitivity to the applied magnetic field. Specific-heat measurements further confirm the phase transition at 48 K, while the relatively large Sommerfeld coefficient ($\gamma = 195.6$ mJ·mol^{-1}·K^{-2}) suggests strong electronic correlations in $Cs_3V_9Te_{13}$. In addition, temperature-dependent X-ray diffraction results indicate no obvious structural change across 48 K. Taken together, these results suggest that the anomaly is not induced by a structural transition but may be associated with an electronic and/or magnetic phase transition. High-pressure transport measurements reveal a highly tunable electronic state in $Cs_3V_9Te_{13}$, while first-principles calculations suggest electronic features reminiscent of kagome systems and an antiferromagnetic tendency that is progressively suppressed under pressure. These results demonstrate that this material, with its structurally novel Reuleaux-triangle-like lattice, serves as a new platform for exploring the interplay between nontrivial lattice geometry and emergent physical phenomena.

The geometry of a crystal lattice plays a central role in shaping electronic structures and emergent quantum states [1]. In condensed-matter systems, lattice geometry provides a powerful route to engineer band topology and dispersion, enabling the realization of Dirac cones, flat bands, and van Hove singularities. Such features can strongly amplify electron correlations and instabilities, making geometrically nontrivial lattices fertile platforms for unconventional superconductivity, topological phases, and other emergent correlated orders [2,3].

Distinct lattice geometries are known to host characteristic and often highly nontrivial physical properties. For instance, the CuO_2 planes in cuprate high-temperature superconductors can be mapped onto a Lieb-lattice framework, supporting flat-band physics and correlation-driven magnetism [4–6]. Kagome lattices, built from corner-sharing triangles, exhibit strong geometric frustration [7–9] and have been extensively studied for quantum spin liquids [10-12], unconventional superconductivity [13–15], and symmetry-breaking electronic orders [16–20]. In contrast, the honeycomb lattice of graphene hosts massless Dirac fermions with linear dispersion, leading to high carrier mobility and rich twist-angle physics in moiré superstructures [21–25]. Platforms for complex magnetism and correlated electronic behavior, as well as potential topological band structures, have been explored in a variety of lattice geometries, including the dice lattice [26,27], the Shastry–Sutherland lattice [28,29], the square-kagome lattice [30,31], and several Archimedean lattices [32–34]. Despite these advances, many novel lattice geometries remain to be explored. In particular, lattices composed of interwoven triangular, square, and pentagonal motifs remain largely unexplored. The interplay among these distinct local geometries may introduce additional frustration, competing interactions, and novel band structures, potentially giving rise to previously inaccessible quantum states.

Here, we report the synthesis of a new layered compound, $Cs_3V_9Te_{13}$, whose V sublattice forms a Reuleaux-triangle-like network composed of triangular, square, and pentagonal motifs. This unusual lattice can also be viewed as a distorted derivative of the CsV_3Sb_5-type structure [35]: instead of preserving the ideal kagome framework, the V network is strongly reconstructed into a Reuleaux-triangle-like arrangement, giving rise to a geometry beyond the conventional "135" family. Such a pronounced structural distortion, together with the modified stoichiometry, is likely associated with the replacement of Sb by Te, which changes both the chemical valence balance and ionic-size matching in the lattice.

Moreover, transport, Hall, magnetic, and specific-heat measurements reveal a possible phase transition near 48 K. The anomaly is insensitive to the applied magnetic field and is not accompanied by detectable structural changes in the temperature-dependent X-ray diffraction (XRD), suggesting a nonstructural transition of likely electronic and/or magnetic origin. Under high pressure, the transport behavior exhibits a nonmonotonic evolution, indicating that the electronic states of $Cs_3V_9Te_{13}$ are highly tunable under lattice compression. These results identify $Cs_3V_9Te_{13}$ as a new platform for exploring the interplay between nontrivial lattice geometry and emergent phenomena.

The Reuleaux triangle [Fig. 1(a)], formed by three equal-radius

Received 18 March 2026; accepted 23 April 2026; published 1 June 2026
© 2026 Chinese Physical Society and IOP Publishing Ltd. All rights, including for text and data mining, AI training, and similar technologies, are reserved.

Check for updates

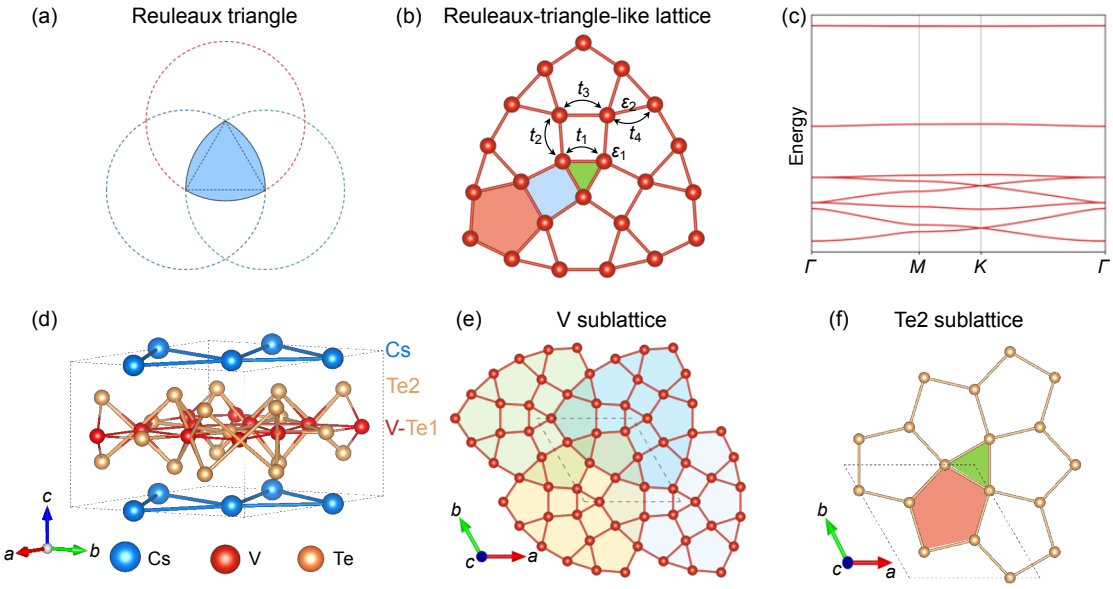

Fig. 1. Reuleaux-triangle-like structural motif in $Cs_3V_9Te_{13}$. (a) Schematic illustration of a Reuleaux triangle. The Reuleaux triangle is shaded in blue and is constructed from three equal-radius circular arcs. (b) Reuleaux-triangle-like lattice motif formed by interconnected triangular, quadrilateral, and pentagonal units, highlighted in green, blue, and red, respectively. t_1, t_2, t_3, t_4 represent atomic nearest-neighbor hoppings; ε_1 and ε_2 represent the on-site energies of two inequivalent atoms. (c) Tight-binding band structure considering nearest-neighbor hoppings calculated for the Reuleaux-triangle lattice along the high-symmetry path. t_1, t_2, t_3, and t_4 are set to −0.30, −0.15, −0.12, and −0.10 eV, respectively. ε_1 and ε_2 are chosen as 6.3 and 5.1 eV, respectively. These parameters are based on the hopping integrals of the V d_{z^2} orbital obtained by the Wannier fitting. (d) Schematic crystal structure of $Cs_3V_9Te_{13}$, with Cs atoms shown in blue, V atoms in red, and Te atoms in yellow. The dashed lines denote the unit cell. (e) Two-dimensional V sublattice in $Cs_3V_9Te_{13}$, highlighting the Reuleaux-triangle-like network. (f) Two-dimensional Te2 sublattice in $Cs_3V_9Te_{13}$, consisting of an arrangement of edge-sharing pentagons and triangles.

circular arcs, is a geometrical figure that preserves the threefold rotational symmetry while maintaining a constant width in all directions and is therefore of fundamental interest in mathematics and engineering design [36,37]. In condensed-matter physics, however, lattices with a Reuleaux-triangle-like geometry have remained largely unexplored. In this spirit, the lattice shown in Fig. 1(b), formed by interconnected triangular, quadrilateral, and pentagonal units, exhibits the characteristic geometry of a Reuleaux triangle and can therefore be described as a Reuleaux-triangle-like lattice. To gain insight into its electronic properties, we calculate the band structure of this lattice using a nearest-neighbor tight-binding model [Fig. 1(c)]. The hopping parameters are set to $t_1 = -0.30$ eV, $t_2 = -0.15$ eV, $t_3 = -0.12$ eV, and $t_4 = -0.10$ eV based on the hopping integrals of the V d_{z^2} orbital obtained by Wannier fitting [Fig. S1 of the Supplementary Material (SM)]. These *ab initio*-derived parameters follow the expected trend of decaying hopping strength with increasing bond length. The on-site energies ε_1 and ε_2 are extracted as 6.3 eV and 5.1 eV, respectively. Notably, the electronic band structure of this lattice closely resembles that of the kagome lattice, hosting a rich variety of exotic electronic states, including massless Dirac points, van Hove singularities with a high density of states (DOS), and flat bands originating from destructive quantum interference.

$Cs_3V_9Te_{13}$ crystallizes in a layered hexagonal structure with space group $P\bar{6}2m$ [Fig. 1(d)], as determined by single-crystal XRD. Detailed crystallographic information is provided in Tables S1–S3 of the SM. Along the c axis, the crystal can be described by a Cs-Te2-V-Te1-Te2-Cs stacking sequence, reminiscent of the layered architecture of CsV_3Sb_5 [35,38]. The crystal structure consists of a highly complex framework built from several intertwined atomic sublattices. The V atoms form a distinctive two-dimensional network of a Reuleaux-triangle-like lattice [Fig. 1(e)]. Furthermore, the V-Te1 layer is sandwiched between two Te2 layers, in which the Te2 atoms form a distinct sublattice composed of edge-sharing pentagons and triangles [Fig. 1(f)]. Together, these intertwined sublattices give rise to the intricate layered framework, highlighting the structural complexity of $Cs_3V_9Te_{13}$ beyond the conventional kagome motif. Notably, $Cs_3V_9Te_{13}$ is stable under ambient conditions and can be mechanically exfoliated, highlighting its potential as a layered material.

The representative XRD pattern of a $Cs_3V_9Te_{13}$ single crystal shows only the (001) peaks [Fig. 2(a)], indicating a preferred orientation along the c axis, as expected for a layered structure. The calculated c-axis lattice parameter is 8.27 Å, which is consistent with the value determined from single-crystal XRD. The inset shows an optical image of a representative single crystal with a regular hexagonal morphology. Energy-dispersive spectroscopy (EDS) analysis of bulk $Cs_3V_9Te_{13}$ yields a semi-quantitative atomic ratio of Cs : V : Te ≈ 3.1 : 9.0 : 13.0, in good agreement with its nominal stoichiometry.

To further confirm this novel structure, atomic-resolution high-angle annular dark-field (HAADF) scanning transmission electron microscopy (STEM) measurements were carried out. The Z-contrast image of $Cs_3V_9Te_{13}$ [Fig. 2(c)], overlaid with the structural model, shows excellent agreement with the proposed structure. The experimental STEM bright-field (BF) image is also consistent with the simulated BF image [Fig. 2(d)], providing further support for the structural model. The selected-area electron diffraction pattern agrees well with the corresponding simulated diffraction pattern along the [120] orientation (Fig. S2 of the SM), confirming the [120] orientation and further supporting the structural assignment. Additional atomic-resolution STEM characterization taken along the [001] and [100] orientations is provided in Figs. S3 and S4 of the SM and further supports the proposed crystal structure. These results collectively demonstrate the high crystallinity, phase purity, and well-defined layered structure of $Cs_3V_9Te_{13}$, providing a solid basis for the subsequent investigation of its physical properties.

The physical properties of $Cs_3V_9Te_{13}$ were further examined through transport and magnetic measurements. As shown in Fig. 3(a), the resistance of the $Cs_3V_9Te_{13}$ single crystal exhibits a non-monotonic temperature dependence, with a hump-like feature. As the temperature increases, the resistivity first increases up to about 100 K and then decreases monotonically. In addition, a weak kink is visible near 48 K, as highlighted in the inset of Fig. 3(a). This anomaly is reminiscent of transport features observed across electronically driven transitions in kagome-related materials such as CsV_3Sb_5 [38]. To visualize the kink clearly, the temperature derivative of the resistivity, $d\rho/dT$,

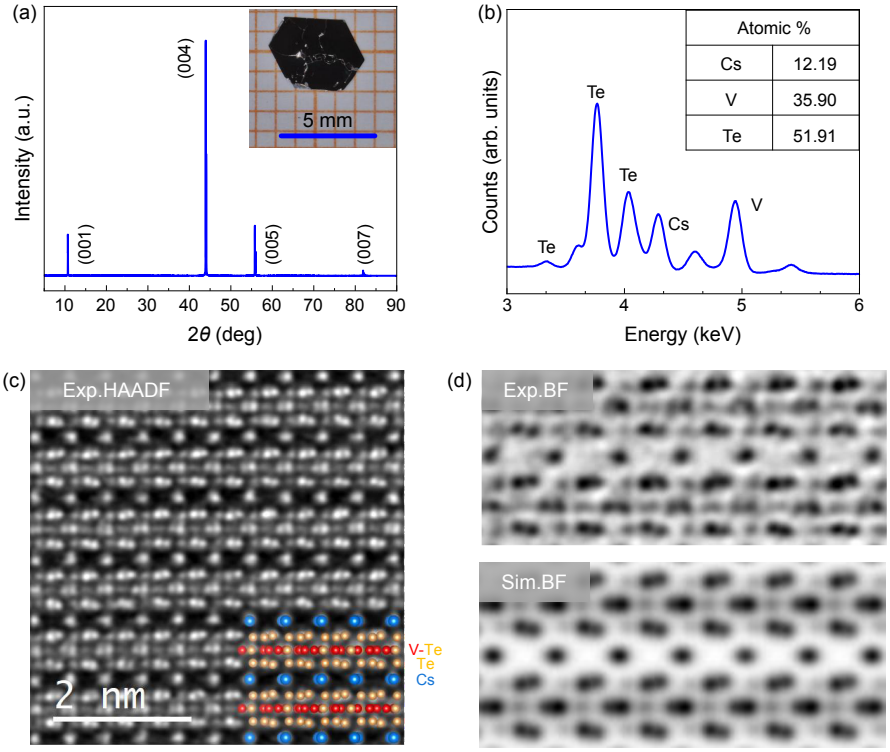

Fig. 2. Structural characterization and compositional analysis of the $Cs_3V_9Te_{13}$ crystal. (a) Single-crystal XRD pattern of $Cs_3V_9Te_{13}$, showing only (00*l*) reflections consistent with its layered structure. The inset shows an optical image of a representative crystal with a regular hexagonal morphology. (b) EDS spectrum and atomic percentage analysis of $Cs_3V_9Te_{13}$, yielding a composition close to the nominal stoichiometry with Cs : V : Te = 3.1 : 9 : 13.0. (c) Atomic-resolution HAADF-STEM image viewed along the [120] zone axis, with the corresponding structural model superimposed, where Cs, V, and Te atoms are represented by blue, red, and yellow spheres, respectively. (d) Experimental and simulated BF-STEM images along the same projection, showing good agreement with the structural model.

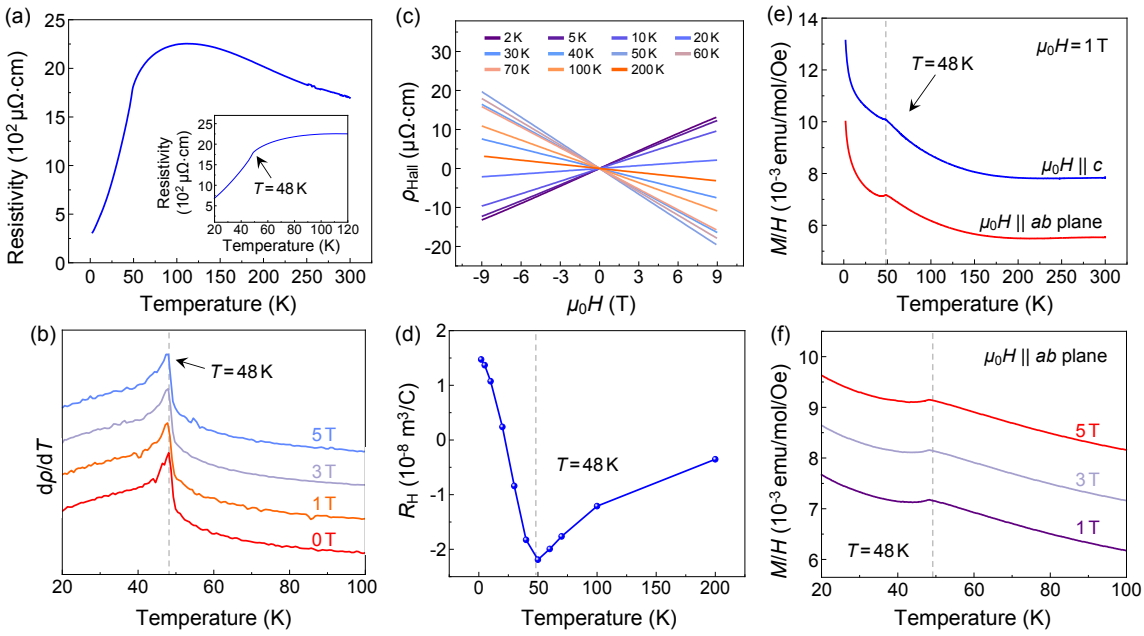

Fig. 3. Electrical transport and magnetic measurement of $Cs_3V_9Te_{13}$ single crystals. (a) Temperature-dependent resistivity of $Cs_3V_9Te_{13}$, showing a non-monotonic temperature dependence with a hump-like feature. The inset presents an enlarged view, where a kink at 48 K can be clearly identified. (b) Temperature derivative of the resistivity, $d\rho/dT$, under different magnetic fields, highlighting a pronounced anomaly at 48 K with weak field dependence. The curves are vertically offset for clarity. (c) Field-dependent Hall resistivity, ρ_{xy}, measured at different temperatures. (d) Temperature dependence of the Hall coefficient, R_H, extracted from linear fits to the Hall resistivity curves. A pronounced minimum is observed, close to the characteristic temperature identified from the resistivity anomaly. (e) Magnetic susceptibility, M/H, measured under $\mu_0 H = 1$ T with the magnetic field applied parallel to the *c* axis and the *ab* plane. Both curves show an anomaly near 48 K. (f) Temperature-dependent M/H measured with $\mu_0 H$ parallel to the *ab* plane under different magnetic fields, indicating that the 48 K anomaly is robust against magnetic fields. The curves are vertically offset for clarity, with a shift of 1×10^{-3} emu/mol/Oe between adjacent curves.

is plotted in Fig. 3(b). There is a pronounced peak at 48 K, corresponding to the kink in the resistance curve. To investigate the evolution of the anomaly under magnetic fields, the field-dependent resistance measurements were carried out. As shown in Fig. 3(b), the peak

remains clearly visible up to 5 T, with no obvious shift in temperature, indicating that the anomaly near 48 K is robust against the applied magnetic fields.

Hall measurements were performed on $Cs_3V_9Te_{13}$ to investigate its charge transport properties, as shown in Fig. 3(c). The Hall resistivity shows an almost linear dependence on the magnetic field at all measured temperatures. Notably, the slope of $\rho(H)$ changes sign with increasing temperature, suggesting a possible crossover of the dominant carrier type from hole-like at low temperatures to electron-like at higher temperatures. By linearly fitting the Hall resistivity curves, the Hall coefficient R_H was extracted and is plotted in Fig. 3(d). The Hall coefficient, R_H, changes sign near 20 K, and a pronounced minimum in $R_H(T)$ is observed around 50 K, close to the characteristic temperature of 48 K identified from the kink in the temperature-dependent resistivity. In a multiband system, the Hall coefficient depends on both carrier densities and mobilities. The observed sign change and nonmonotonic temperature dependence of R_H suggest the coexistence of multiple types of carriers and a redistribution of their relative contributions across the anomaly. This result indicates that the anomaly is accompanied by a change in the carrier response, likely involving a redistribution of the relative contributions from different carriers through changes in mobility and/or carrier density, or a change in the electronic structure.

The magnetic properties were further investigated by temperature-dependent magnetization measurements. Under $\mu_0 H = 1$ T, the magnetic susceptibility of $Cs_3V_9Te_{13}$ exhibits a monotonic decrease with increasing temperature for magnetic fields applied along the c axis and the ab plane [Fig. 3(e)]. A distinct kink appears at $T \approx 48$ K, which is consistent with the resistance measurements. To further analyze the magnetic response of $Cs_3V_9Te_{13}$, the high-temperature susceptibility between 60 and 130 K was fitted with the modified Curie–Weiss law, $\chi = \chi_0 + C/(T - \theta_W)$, where χ_0, C, and θ_W are the temperature-independent susceptibility, Curie constant, and Weiss temperature, respectively. As shown in Fig. S5 of the SM, $1/(\chi - \chi_0)$ displays an approximately linear temperature dependence within the fitting range. The fit yields Weiss temperatures of $\theta_W = -61.5$ K for $H \parallel ab$ and $\theta_W = -47.0$ K for $H \parallel c$. The negative Weiss temperature indicates dominant antiferromagnetic correlations in this compound. The modified Curie–Weiss fit yields an effective moment of $1.73\mu_B$ per formula unit for $H \parallel ab$, corresponding to about $0.58\mu_B$ per V atom. Such a reduced effective moment may suggest that the magnetism is not well described by a fully localized-moment picture. Consistently, the isothermal magnetization $M(H)$ curves measured at various temperatures for both $H \parallel c$ and $H \parallel ab$ are nearly linear up to 5 T and show no detectable hysteresis (Fig. S6 of the SM), indicating the absence of ferromagnetic ordering in the measured temperature range. Furthermore, the zero field cooling curves measured under different magnetic fields [Fig. 3(f)] reveal no obvious suppression of the kink, in good agreement with the resistivity data. Combined with the transport anomaly at the same temperature, these results reveal a possible phase transition that is robust against the applied magnetic fields.

Specific-heat measurements further reveal a phase transition at 48 K, as shown in Fig. S7 of the SM. A pronounced λ-shaped anomaly is observed at this temperature (Fig. S7a of the SM), providing clear evidence for a thermodynamic phase transition, consistent with the resistivity and magnetic susceptibility results discussed above. To extract the relevant low-temperature parameters, the specific-heat data were analyzed using the expression $C = \gamma T + \beta T^3$, where γT and βT^3 represent the electronic and phonon contributions, respectively. As shown in Fig. S7b of the SM, a linear fit of C/T versus T^2 in the 2–8 K range gives a Sommerfeld coefficient of $\gamma = 195.6$ mJ·mol^{-1}·K^{-2} and $\beta = 10.6$ mJ·mol^{-1}·K^{-4}. By using the relation $\Theta_D = [12\pi^4 nR/(5\beta)]^{1/3}$, the Debye temperature was estimated to be 166 K. The relatively large γ value, which is substantially higher than those of conventional metals and also much larger than that reported for the kagome superconductor CsV_3Sb_5 (20.03 mJ·mol^{-1}·K^{-2}) [39], suggests pronounced electronic correlations in this system. Notably, this value is about one-half of that reported for LiV_2O_4 (420 mJ·mol^{-1}·K^{-2}) [40], indicating that $Cs_3V_9Te_{13}$ lies in an intermediate regime between kagome vanadium metals and strongly correlated systems. This comparison suggests that the interesting electron correlations in $Cs_3V_9Te_{13}$ merit further investigation. In addition, the entropy change associated with the transition was estimated to be $\Delta S = 0.43$ J·mol^{-1}·K^{-1}. Such a small entropy release is too small to support the full ordering of localized moments. Instead, it is comparable to those reported for metals undergoing a charge-density-wave (CDW) transition, such as 2H-$NbSe_2$ (0.6 J·mol^{-1}·K^{-1}) [41] and CuTe (0.27 J·mol^{-1}·K^{-1}) [42]. Therefore, this relatively small entropy change suggests that the transition in $Cs_3V_9Te_{13}$ is more likely associated with an electronic and/or magnetic transition rather than the full ordering of localized moments.

The resistivity, magnetic susceptibility, and specific-heat measurements all exhibit a clear anomaly near 48 K. To further determine whether this anomaly is accompanied by a structural change, temperature-dependent XRD measurements were performed. The diffraction patterns collected at 40 K and 100 K along several crystallographic directions are shown in Fig. S8 of the SM, including the $0kl$, $h0l$, and $hk0$ reciprocal-space planes. A comparison of the diffraction patterns collected at 40 K and 100 K reveals no discernible change, suggesting that the anomaly near 48 K is not associated with a structural phase transition. In addition, because a conventional long-range CDW transition is typically accompanied by lattice modulation and superlattice reflections [43], the absence of clear extra diffraction spots argues against a CDW-like transition with pronounced structural modulation. Therefore, considering the weak field dependence observed in both resistivity and magnetization, these results suggest that the anomaly at 48 K is more likely of an electronic and/or magnetic origin.

To further explore the tunability of the physical properties in $Cs_3V_9Te_{13}$, we performed high-pressure transport measurements. As shown in Figs. 4(a) and 4(b), the semiconducting hump-like feature observed above 100 K in resistance at ambient pressure is rapidly suppressed at 1.5 GPa, although a broad hump is still present and the sample exhibits metallic behavior. When the pressure increases to 9 GPa, the resistance gradually decreases and the hump nearly disappears, indicating that the transport properties of $Cs_3V_9Te_{13}$ are highly sensitive to pressure. With further increasing pressure, the low-temperature resistance exhibits a nonmonotonic evolution and gradually increases. For a better visualization of the resistance under high pressure, we constructed a temperature–pressure phase diagram and the background color represents the resistance value, as shown in Fig. 4(c). At low pressures, the resistance is comparatively high and gradually reaches a minimum region as the pressure increases to 12.5 GPa. However, the resistance increases again above 16 GPa, suggesting that the metallicity is subsequently weakened. To further reveal whether the nonmonotonic evolution of resistance is accompanied by a structural phase transition, we performed high-pressure XRD measurements.

The room-temperature XRD patterns of $Cs_3V_9Te_{13}$ under various pressures up to 24.52 GPa are shown in Fig. 4(d) and Fig. S9 of the SM. No diffraction peak splitting or extra peaks were observed under high pressure (Fig. S9a of the SM), which rules out the occurrence of any structural phase transition in the measured pressure range. As displayed in Fig. 4(d) and Fig. S9b of the SM, the pressure dependences of lattice parameters a, c, and volume V were obtained by using the LeBail fit to XRD patterns. Here, we can see that the c axis is more compressible than the a axis, i.e., the c axis is reduced by 18.72% whereas the a axis shrinks by 7.29% to 24.52 GPa, which is expected for a layered structure. The continuous reduction of $V(P)$ can be fitted well with the Birch–Murnaghan equation, which gives the bulk modulus $B_0 = 31.38$ GPa and $V_0 = 731.5$ Å^3.

Overall, the non-monotonic evolution of the resistance of $Cs_3V_9Te_{13}$ highlights the high tunability of its physical properties, and high-pressure XRD measurements suggest that this behavior is more likely related to changes in the electronic state. Moreover, it likely reflects a complex interplay between lattice compression and electronic

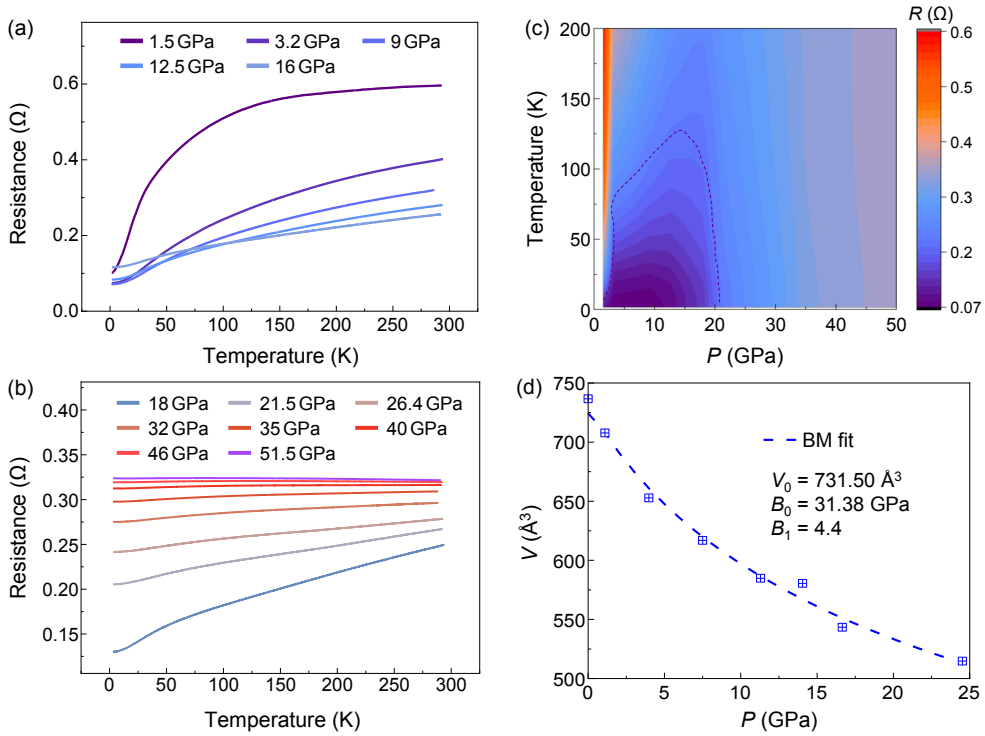

Fig. 4. Pressure-dependent resistance and XRD measurements of $Cs_3V_9Te_{13}$. (a) and (b) Temperature-dependent resistance of $Cs_3V_9Te_{13}$ measured under different pressures, showing that the metallic character is first enhanced and then suppressed with increasing pressure. (c) Temperature–pressure contour plot of the resistance. The dashed line is a guide to the eye outlining the low-resistance region, illustrating the non-monotonic pressure dependence of the metallicity. (d) Pressure dependence of volume V. The dashed line represents the fit to the Birch–Murnaghan equation.

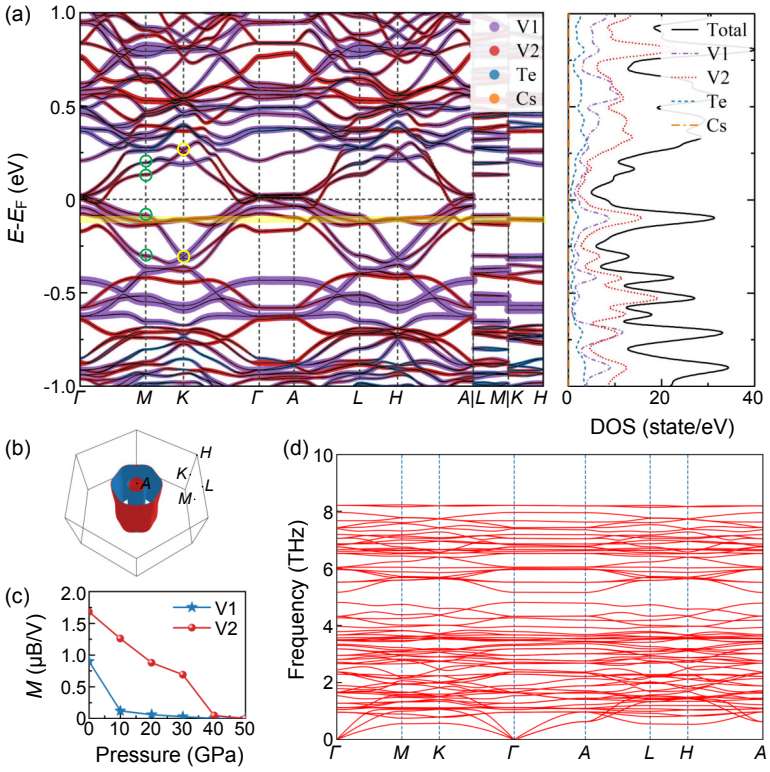

Fig. 5. Calculated electronic properties of $Cs_3V_9Te_{13}$. (a) Left panel: Electronic band structure of $Cs_3V_9Te_{13}$ projected onto different atomic orbitals with SOC. Right panel: Corresponding partial DOS projected onto different atoms. The van Hove singularities and the Dirac points near the Fermi level are marked with green and yellow circles, respectively. The flat band near $E - E_F \approx -0.08$ eV is indicated by a yellow shaded stripe. (b) Three-dimensional Fermi surface of $Cs_3V_9Te_{13}$, exhibiting cylindrical characteristics. (c) Evolution of the magnetic moments of V atoms as a function of applied pressure. (d) Calculated phonon spectrum of $Cs_3V_9Te_{13}$ at ambient pressure.

states. The above results suggest that high pressure provides an effective route to manipulate the metallic behavior of $Cs_3V_9Te_{13}$. Other approaches, such as chemical doping or intercalation, are also worth further investigation.

Figure 5(a) illustrates the first-principles electronic band structure of $Cs_3V_9Te_{13}$ projected onto the atomic orbitals with spin–orbit coupling (SOC) considered. Our analysis of various magnetic configurations indicates that the energetically favored state is an antiferromagnetic structure characterized by in-plane ferromagnetism and interlayer antiferromagnetism. Calculations incorporating SOC with different magnetization directions indicate an easy axis along the a direction, yielding a magnetic anisotropy energy of approximately 1.5 meV/f.u. The calculated magnetic moments for the two inequivalent V atoms (V1 and V2) are $0.87\mu_B$ and $1.65\mu_B$, respectively. With increasing pressure, these magnetic moments gradually diminish and completely vanish at around 40 GPa. The calculated suppression of magnetic moments under pressure suggests that magnetic correlations may be weakened upon compression, which could be relevant to the pressure-dependent evolution of the transport behavior.

As shown in the projected band structure [Fig. 5(a)], the electronic states near the Fermi level (E_F) predominantly arise from the V atoms. Notably, multiple Dirac points are observed at the K (H) points, while several van Hove singularities emerge at the M (L) points near E_F [green and yellow circles in Fig. 5(a)]. In addition, several bands exhibit relatively flat dispersion throughout the entire Brillouin zone. These features are consistent with the tight-binding model results shown in Fig. 1(c), indicating that the Reuleaux-triangle-like lattice hosts Dirac-, van Hove-, and flat-band-related electronic features reminiscent of kagome systems. Detailed orbital-projected band structures reveal strong hybridization among different d orbitals of the V atoms, as shown in Figs. S10 and S11 of the SM. The Fermi surface depicted in Fig. 5(b) exhibits cylindrical characteristics, which aligns with the weak band dispersion along the k_z direction observed in Fig. 5(a), reflecting the 2D nature of the electronic structure driven by the interlayer van der Waals interactions. Furthermore, the relatively small Fermi surface and the dip in the DOS near E_F are consistent with the modest metallic character observed experimentally. Moreover, the absence of imaginary phonon modes in the calculated phonon spectrum [Fig. 5(d)] indicates that the ambient-pressure structure is dynamically stable, which is consistent with the lack of evidence for a structural transition from the temperature-dependent XRD measurements.

In summary, we have synthesized a new layered vanadium-based compound, $Cs_3V_9Te_{13}$, whose crystal structure features a distinctive Reuleaux-triangle-like vanadium sublattice. The structural analysis shows that the compound has a layered structure with several intertwined atomic sublattices. At ambient pressure, the transport, Hall, and magnetic measurements consistently reveal an anomaly near 48 K, suggesting a possible phase transition. The specific heat data also reveal a phase transition at 48 K, and the relatively large Sommerfeld coefficient ($\gamma = 195.6$ mJ·mol^{-1}·K^{-2}) indicates the presence of strong electronic correlations in this system. Temperature-dependent XRD measurements show no discernible structural change across this temperature range, indicating that the anomaly is not accompanied by any obvious structural transition. Taken together, these results suggest a nonstructural transition of likely electronic and/or magnetic origin. Furthermore, the high-pressure transport measurements reveal a non-monotonic evolution of metallicity, highlighting the strong tunability of the electronic state under lattice compression. Our theoretical calculations reveal a quasi-2D electronic structure with kagome-related features and indicate that an antiferromagnetic configuration is energetically favored, with the calculated magnetic moments gradually suppressed under pressure. These results demonstrate $Cs_3V_9Te_{13}$ as a new platform for exploring the interplay between nontrivial lattice geometry, correlated electronic behavior, and emergent phase transitions.

Single Crystal Growth of $Cs_3V_9Te_{13}$. Single crystals of $Cs_3V_9Te_{13}$ were grown from Cs liquid (purity 99.98%), V powder (purity 99.9%), and Te shots (purity 99.999%) via a self-flux method. The mixture was placed into an alumina crucible and sealed in a quartz ampoule under an argon atmosphere. The mixture was heated to 1000 ℃ and soaked for 24 h, and subsequently cooled to 600 ℃ at 2 ℃/h. Finally, the flux was removed by centrifugation at 600 ℃, and crystals with regular morphology and metallic luster were obtained. Due to the high reactivity of the alkali metals, all weighing procedures were carried out in a glovebox under an atmosphere with $O_2 < 0.01$ ppm and $H_2O < 0.01$ ppm. The stoichiometric ratio of $Cs_3V_9Te_{13}$ was confirmed by scanning electron microscopy (SEM) and energy-dispersive X-ray spectroscopy.

Sample Characterization. XRD patterns were collected using a Rigaku SmartLab SE X-ray diffractometer with Cu Kα radiation ($\lambda = 0.15418$ nm) at room temperature. Single-crystal XRD and temperature-dependent XRD measurements were carried out using a Bruker D8 diffractometer. SEM and EDS analyses were performed using a HITACHI S5000 equipped with an energy-dispersive analysis system, Bruker XFlash 6|60. Magnetic susceptibility was determined by a SQUID magnetometer (Quantum Design MPMS XL-1). Electrical resistivity data were collected on a Quantum Design Physical Properties Measurement System (PPMS). The cross-sectional sample along the [120] projection was prepared using a focused ion beam system. Atomic-scale STEM imaging was carried out on an aberration-corrected Nion U-HERMES 100 dedicated STEM, operated at an acceleration voltage of 60 kV.

First-Principles Calculations. All density functional theory (DFT) simulations were executed via the VASP code [44]. We employed the Perdew–Burke–Ernzerhof [45] generalized gradient approximation to describe the exchange and correlation effects. A plane-wave cutoff energy of 520 eV and a Γ-centered k-point sampling of $6\times6\times8$ were chosen to ensure numerical accuracy. The geometry relaxation was performed until the energy and force convergence limits tightly reached 10^{-7} eV/atom and 1 meV/Å, respectively. Additionally, phonon properties and vibrational modes were computed using the finite displacement method as implemented in the phonopy software [46], utilizing the DFT-derived force constants. The Wannier90 package [47] was utilized to construct maximally localized Wannier functions and extract hopping parameters by including all V d and Te p orbitals.

High-Pressure Electrical Property Measurements. High-pressure electrical transport measurements of $Cs_3V_9Te_{13}$ were performed in a BeCu-type diamond anvil cell (DAC) with 300 μm flat by employing the standard four-probe method. KBr was used as the solid pressure-transmitting medium. The size of the single-crystal samples was about $60 \times 20 \times 10$ μm^3.

High-Pressure Powder XRD Measurements. The powder XRD measurements were performed under various pressures up to 24.5 GPa with a symmetric DAC in a laboratory X-ray diffractometer at room temperature, Rigaku XtaLAB Synergy R, equipped with Mo Kα ($\lambda = 0.71073$ Å) radiation. The pressure values were determined by ruby fluorescence.

Author Contributions

H.-J.G. designed the project. H.T.Y., H.G., and Z.Z. prepared the samples. Z.Z., R.W.W., H.S.L., and H.T.Y. performed the magnetization measurement and the transport experiments. X.W.Y., and S.G. performed DFT calculations. J.P.S., L.Z., and J.G.C. performed the pressure-related measurements. Y.H.Z., and H.Z. performed the specific-heat measurements, L.H.B., and X.L. performed the EDS measurements. T.L., and W.Z. performed the STEM measurements. J.P.S, H.M.M., X.L.M, and X.H.Y. performed the High-pressure XRD measurements. All authors participated in the data analysis and manuscript writing.

Competing Interests

The authors declare that they have no competing interests.

Data Availability

Data measured or analyzed during this study are available from

the corresponding authors on reasonable request.

Acknowledgements

The work was supported by the National Key Research and Development Projects of China (Grant Nos. 2022YFA1204100, 2023YFA1406100, and 2024YFA1207800), the National Natural Science Foundation of China (Grant Nos. 62488201, 52572188, 12522407, and U23A6015), the Chinese Academy of Sciences (Grant Nos. YSBR-003 and YSBR-053), and the Innovation Program of Quantum Science and Technology (Grant No. 2021ZD0302700). The high-pressure XRD measurements were performed at the High-pressure synergetic measurement station of Synergic Extreme Condition User Facility (SECUF) (https://cstr.cn/31123.02.SECUF).

References

[1] Regnault N, Xu Y, Li M R, Ma D S, Jovanovic M, Yazdani A, Parkin S S P, Felser C, Schoop L M, Ong N P, Cava R J, Elcoro L, Song Z D, and Bernevig B A 2022 *Nature* **603** 824
[2] Beugeling W, Everts J C, and Morais Smith C 2012 *Phys. Rev. B* **86** 195129
[3] Leykam D, Andreanov A, and Flach S 2018 *Adv. Phys.: X* **3** 1473052
[4] Lieb E H 1989 *Phys. Rev. Lett.* **62** 1201
[5] Mielke A 1991 *J. Phys. A: Math. Gen.* **24** 3311
[6] Weeks C and Franz M 2010 *Phys. Rev. B* **82** 85310
[7] Yin J X, Ma W, Cochran T A, Xu X, Zhang S S, Tien H J, Shumiya N, Cheng G, Jiang K, Lian B, Song Z, Chang G, Belopolski I, Multer D, Litskevich M, Cheng Z J, Yang X P, Swidler B, Zhou H, Lin H, Neupert T, Wang Z, Yao N, Chang T R, Jia S, and Zahid Hasan M 2020 *Nature* **583** 533
[8] Yin J X, Zhang S S, Li H, Jiang K, Chang G, Zhang B, Lian B, Xiang C, Belopolski I, Zheng H, Cochran T A, Xu S Y, Bian G, Liu K, Chang T R, Lin H, Lu Z Y, Wang Z, Jia S, Wang W, and Hasan M Z 2018 *Nature* **562** 91
[9] Morali N, Batabyal R, Nag P K, Liu E, Xu Q, Sun Y, Yan B, Felser C, Avraham N, and Beidenkopf H 2019 *Science* **365** 1286
[10] Savary L and Balents L 2016 *Rep. Prog. Phys.* **80** 16502
[11] Broholm C, Cava R J, Kivelson S A, Nocera D G, Norman M R, and Senthil T 2020 *Science* **367** eaay0668
[12] Khuntia P, Velazquez M, Barthélemy Q, Bert F, Kermarrec E, Legros A, Bernu B, Messio L, Zorko A, and Mendels P 2020 *Nat. Phys.* **16** 469
[13] Liu Y, Liu Z Y, Bao J K, Yang P T, Ji L W, Wu S Q, Shen Q X, Luo J, Yang J, Liu J Y, Xu C C, Yang W Z, Chai W L, Lu J Y, Liu C C, Wang B S, Jiang H, Tao Q, Ren Z, Xu X F, Cao C, Xu Z A, Zhou R, Cheng J G, and Cao G H 2024 *Nature* **632** 1032
[14] Chen H, Yang H, Hu B, Zhao Z, Yuan J, Xing Y, Qian G, Huang Z, Li G, Ye Y, Ma S, Ni S, Zhang H, Yin Q, Gong C, Tu Z, Lei H, Tan H, Zhou S, Shen C, Dong X, Yan B, Wang Z, and Gao H J 2021 *Nature* **599** 222
[15] Deng H, Qin H, Liu G, Yang T, Fu R, Zhang Z, Wu X, Wang Z, Shi Y, Liu J, Liu H, Yan X Y, Song W, Xu X, Zhao Y, Yi M, Xu G, Hohmann H, Holbæk S C, Dürrnagel M, Zhou S, Chang G, Yao Y, Wang Q, Guguchia Z, Neupert T, Thomale R, Fischer M H, and Yin J X 2024 *Nature* **632** 775
[16] Guo C, Putzke C, Konyzheva S, Huang X, Gutierrez-Amigo M, Errea I, Chen D, Vergniory M G, Felser C, Fischer M H, Neupert T, and Moll P J W 2022 *Nature* **611** 461
[17] Li H, Zhao H, Ortiz B R, Park T, Ye M, Balents L, Wang Z, Wilson S D, and Zeljkovic I 2022 *Nat. Phys.* **18** 265
[18] Mielke C, Das D, Yin J X, Liu H, Gupta R, Jiang Y X, Medarde M, Wu X, Lei H C, Chang J, Dai P, Si Q, Miao H, Thomale R, Neupert T, Shi Y, Khasanov R, Hasan M Z, Luetkens H, and Guguchia Z 2022 *Nature* **602** 245
[19] Yang H, Ye Y, Zhao Z, Liu J, Yi X W, Zhang Y, Xiao H, Shi J, You J Y, Huang Z, Wang B, Wang J, Guo H, Lin X, Shen C, Zhou W, Chen H, Dong X, Su G, Wang Z, and Gao H J 2024 *Nat. Commun.* **15** 9626
[20] Xing Y, Bae S, Ritz E, Yang F, Birol T, Capa Salinas A N, Ortiz B R, Wilson S D, Wang Z, Fernandes R M, and Madhavan V 2024 *Nature* **631** 60
[21] Castro Neto A H, Guinea F, Peres N M R, Novoselov K S, and Geim A K 2009 *Rev. Mod. Phys.* **81** 109
[22] Bistritzer R and MacDonald A H 2011 *Proc. Natl. Acad. Sci.* **108** 12233
[23] Cao Y, Fatemi V, Fang S, Watanabe K, Taniguchi T, Kaxiras E, and Jarillo-Herrero P 2018 *Nature* **556** 43
[24] Cao Y, Fatemi V, Demir A, Fang S, Tomarken S L, Luo J Y, Sanchez-Yamagishi J D, Watanabe K, Taniguchi T, Kaxiras E, Ashoori R C, and Jarillo-Herrero P 2018 *Nature* **556** 80
[25] Hao Z, Zimmerman A M, Ledwith P, Khalaf E, Najafabadi D H, Watanabe K, Taniguchi T, Vishwanath A, and Kim P 2021 *Science* **371** 1133
[26] Sutherland B 1986 *Phys. Rev. B* **34** 5208
[27] Möller G and Cooper N R 2012 *Phys. Rev. Lett.* **108** 45306
[28] Läuchli A, Wessel S, and Sigrist M 2002 *Phys. Rev. B* **66** 14401
[29] Ferrari F and Valentí R 2024 *Phys. Rev. B* **110** 205140
[30] Lugan T, Jaubert L D C, and Ralko A 2019 *Phys. Rev. Res.* **1** 33147
[31] Fujihala M, Morita K, Mole R, Mitsuda S, Tohyama T, Yano S, Yu D, Sota S, Kuwai T, Koda A, Okabe H, Lee H, Itoh S, Hawai T, Masuda T, Sagayama H, Matsuo A, Kindo K, Ohira-Kawamura S, and Nakajima K 2020 *Nat. Commun.* **11** 3429
[32] Martinez J 1973 *Algebra Univ.* **3** 247
[33] Eddi A, Decelle A, Fort E, and Couder Y 2009 *EPL* **87** 56002
[34] Okabe R, Cheng M, Chotrattanapituk A, Mandal M, Mak K, Córdova Carrizales D, Hung N T, Fu X, Han B, Wang Y, Xie W, Cava R J, Jaakkola T S, Cheng Y, and Li M 2026 *Nat. Mater.* **25** 223
[35] Ortiz B R, Gomes L C, Morey J R, Winiarski M, Bordelon M, Mangum J S, Oswald I W H, Rodriguez-Rivera J A, Neilson J R, Wilson S D, Ertekin E, McQueen T M, and Toberer E S 2019 *Phys. Rev. Mater.* **3** 094407
[36] Shen Z and Wu J 2022 *J. Appl. Phys.* **131** 225101
[37] Fei J, Zhang X, Zhang Q, Yang Y, Wang Z, Deng C, Huang Y, and Wang T 2024 *Front. Optoelectron.* **17** 27
[38] Ortiz B R, Teicher S M L, Hu Y, Zuo J L, Sarte P M, Schueller E C, Abeykoon A M M, Krogstad M J, Rosenkranz S, Osborn R, Seshadri R, Balents L, He J, and Wilson S D 2020 *Phys. Rev. Lett.* **125** 247002
[39] Duan W, Nie Z, Luo S, Yu F, Ortiz B R, Yin L, Su H, Du F, Wang A, Chen Y, Lu X, Ying J, Wilson S D, Chen X, Song Y, and Yuan H 2021 *Sci. China Phys. Mech. Astron.* **64** 107462
[40] Kondo S, Johnston D C, Swenson C A, Borsa F, Mahajan A V, Miller L L, Gu T, Goldman A I, Maple M B, Gajewski D A, Freeman E J, Dilley N R, Dickey R P, Merrin J, Kojima K, Luke G M, Uemura Y J, Chmaissem O, and Jorgensen J D 1997 *Phys. Rev. Lett.* **78** 3729
[41] Eremenko V, Sirenko V, Ibulaev V, Bartolomé J, Arauzo A, and Reményi G 2009 *Physica C* **469** 259
[42] Kuo C N, Huang R Y, Kuo Y K, and Lue C S 2020 *Phys. Rev. B* **102** 155137
[43] Hu Y, Wu X, Ortiz B R, Han X, Plumb N C, Wilson S D, Schnyder A P, and Shi M 2022 *Phys. Rev. B* **106** L241106
[44] Kresse G and Furthmüller J 1996 *Phys. Rev. B* **54** 11169
[45] Perdew J P, Burke K, and Ernzerhof M 1996 *Phys. Rev. Lett.* **77** 3865
[46] Togo A and Tanaka I 2015 *Scr. Mater.* **108** 1
[47] Mostofi A A, Yates J R, Lee Y S, Souza I, Vanderbilt D, and Marzari N 2008 *Comput. Phys. Commun.* **178** 685